# Field measurements of fracture characteristics on a wave-cut platform

Thomas Loriaux[1], James Verdon[2], J.-Michael Kendall[3], Alan Baird[4], and James Wookey[2]


## Abstract

We have used seismic refraction surveys of a wave-cut platform from a field site in South West England to characterize the impact of natural fracture networks on seismic velocities and anisotropy. Time-lapse surveys were performed as the high tide ebbed to investigate the seismic effects of the water draining from the rock. We also deployed a drone to map the fracture sets from the air. Azimuthal variations in the P- and S-wave velocities reflect the orientation of the main east–west-oriented joint set. Seismic velocities increased as the water drained, an effect attributed to a reduction in the effective density of the medium. The ratio of fracture normal ($Z_N$) to tangential ($Z_T$) compliance ($\Omega = Z_N/Z_T$), which can be used as a proxy for fracture saturation and permeability, was observed to increase from $\Omega = 0.18$ to $\Omega = 0.48$, primarily driven by a drop in $Z_T$. These variations are attributed to a decrease in the water content of the main fracture set as the tide retreats.


## Introduction

Fractures can control and enhance the permeability and porosity of a material. Thus, fractures can help in the migration of fluids in geologic reservoirs, such as magma in volcanic settings, water in geothermal fields, or hydrocarbons in sedimentary rocks (Jupe et al., 2003; Vlahovic et al., 2003; Harris et al., 2005; Tang et al., 2005; Khelifa et al., 2014). Fracture-related fluid flow is of crucial concern in the development of underground waste storage (Stork et al., 2015) and hydraulic fracture stimulation (Verdon and Wüstefeld, 2013).

Seismic methods are used to image factures in situ in the subsurface. Reflection seismology is a commonly used method for fracture imaging in hydrocarbon reservoirs (Lynn and Thomsen, 1990). Seismic refraction can be used to image fractures in the shallow surface (Hobday and Worthington, 2012; Foord et al., 2015). Finally, monitoring of microseismicity provides a passive method for fracture characterization (Teanby et al., 2004).

Aligned fractures create seismic anisotropy, i.e., the dependence of the velocity of the seismic waves with the direction of propagation and/or polarization. This effect of fracture networks on seismic wavespeeds is controlled by the fracture compliance, which can be resolved into their normal and tangential (or shear) components $Z_N$ and $Z_T$, respectively (Schoenberg and Sayers, 1995). The fracture compliance ratio $\Omega = Z_N/Z_T$ is an effective indicator of fluid content and permeability in fractured media (Verdon and Wüstefeld, 2013; Foord et al., 2015). However, interpreting fracture compliance is not an easy task because it can be influenced by various fracture properties, such as the internal architecture, connectivity with other fractures and pore spaces, and fluid viscosity. A review of existing $\Omega$ measurements has been published by Verdon and Wüstefeld (2013) and updated by Choi et al. (2014) and Foord et al. (2015). Most of the published data are derived from laboratory experiments made on core samples (Macbeth and Schuett, 2007; Angus et al., 2009) or synthetic samples (Rathore and Fjaer, 1994; Far et al., 2014). As noted by Worthington and Lubbe (2007), field measurements are important in addressing upscaling concerns.

Here, we investigate azimuthal seismic anisotropy using a hammer source to acquire shallow refraction profiles on an exposed wave-cut platform. The rock is exposed at the surface so that fracture attributes, such as strike, length, intensity, and spacing, can be mapped and quantified using an unmanned aerial vehicle (drone). We use these observations to constrain the rock-physics model and better interpret the source of anisotropy. Furthermore, we acquired the surveys as the tide was ebbing, so fluid was draining from

[1]Centro de Estudios Científicos, Valdivia, Chile and University of Bristol, School of Earth Sciences, Bristol BS8 1RJ, UK. E-mail: thomas@cecs.cl (corresponding author).
[2]University of Bristol, School of Earth Sciences, Bristol BS8 1RJ, UK. E-mail: james.verdon@bristol.ac.uk; j.wookey@bristol.ac.uk.
[3]University of Bristol, School of Earth Sciences, Bristol BS8 1RJ, UK and University of Oxford, Department of Earth Sciences, Oxford, UK. E-mail: gljmk@bristol.ac.uk.
[4]NORSAR, Kjeller, Norway. E-mail: alan.baird@bristol.ac.uk.
Manuscript received by the Editor 25 June 2020; revised manuscript received 5 November 2020; published ahead of production 2 February 2021.
This paper appears in *Interpretation*, Vol. 9, No. 2 (May 2021); p. 1–10, 8 FIGS., 1 TABLE.
http://dx.doi.org/10.1190/INT-2020-0132.1. 

the outcrop, allowing an assessment of the effects of fluid saturation on fracture compliance.

## Methods

### *Inversion of measured seismic velocities for fracture compliance*

Anisotropy is caused not only by aligned fracture sets but also by other mechanisms such as grain alignment (Johansen et al., 2004), crystal preferred orientation (Valcke et al., 2006), and sedimentary layering (Bakulin, 2003). Therefore, the observed anisotropy must be related to its causal feature using rock-physics models (e.g., Kendall et al., 2007; Verdon et al., 2009).

Fracture compliance parameters can be inverted from seismic measurements made on the fractured medium (Bakulin et al., 2000; Verdon et al., 2009; Al-Harrasi et al., 2011; Verdon and Kendall, 2011; Wuestefeld et al., 2011; Kendall et al., 2012). To predict the behavior of seismic waves in a fractured medium, a rock-physics model is constructed, in which fractures are embedded in a background material. Fracture parameters include orientation, density, and the nature of the fill material. In our study, the model construction is based on the widely used additional compliance approach introduced by Schoenberg and Sayers (1995), which considers fractures as poorly bonded interfaces representing displacement discontinuities. The overall compliance of a fractured medium ($\mathbf{S}$) can be represented as the sum of the compliance of the intact background ($\mathbf{S}_b$) and the fracture compliance ($\mathbf{S}_f$) as

$$\mathbf{S} = \mathbf{S}_b + \mathbf{S}_f, \tag{1}$$

where $\mathbf{S}$, $\mathbf{S}_b$, and $\mathbf{S}_f$ are the fourth-order $3\times3\times3\times3$ tensors. The additional compliance due to a single set of vertical fractures striking in the $x_1$-$x_3$ plane is given as (written in Voigt notation representing the symmetric $3\times3\times3\times3$ tensor as a $6\times6$ tensor)

$$\mathbf{S}_f = \begin{pmatrix} Z_N & 0 & 0 & 0 & 0 & 0 \\ 0 & 0 & 0 & 0 & 0 & 0 \\ 0 & 0 & 0 & 0 & 0 & 0 \\ 0 & 0 & 0 & 0 & 0 & 0 \\ 0 & 0 & 0 & 0 & Z_T & 0 \\ 0 & 0 & 0 & 0 & 0 & Z_T \end{pmatrix}. \tag{2}$$

The additional compliance of a fracture set of arbitrary orientation can be achieved by rotating $\mathbf{S}_f$. In the case of more than one set of fractures, with different orientations, more than one additional compliance tensor can be added to compute $\mathbf{S}$. Once the compliance tensor is computed, it is inverted to give the stiffness tensor $\mathbf{C}$ that is used in the Christoffel equation to compute P- and S-wave velocities as a function of azimuth. We do so using the MSAT MSphasevels function described by Walker and Wookey (2012). To find the best-fitting model, an inversion is performed by doing a grid search over the crack density, $\xi$, and $Z_N/Z_T$ to find the values that minimize the root-mean-square (rms) misfit between the measured and modeled velocities.

### *Lilstock Beach*

The study area is a beach situated on the southern shore of the Bristol Channel Basin (BCB), near the locality of Lilstock, South West England. It is part of a 20 km long exposed shore of the Mesozoic Blue Lias Formation, consisting of alternating layers of limestone and shale (Engelder and Peacock, 2001). The BCB experiences one of the largest tidal ranges in the world (Xia et al., 2010), which provides excellent coastal exposure, consisting of up to 500 m wide wave-cut platforms and 20 m high cliff sections. The formation of the BCB can be summarized in three main stages, the first being basin extension, with burial and diagenesis (Nemčok et al., 1995). Second, a basin inversion took place, initiated by the Alpine Orogenic collision, including amplification of the folding initially formed during extension (Dart et al., 1995). The BCB was finally uplifted and exhumed, resulting in the present-day configuration (Van Hoorn, 1987). Major tectonic features formed during the basin inversion, with long joints striking subnormal to the compression axis (Engelder and Peacock, 2001). Posterior sets of smaller joints formed after the inversion, and they mostly consist of noncross-cutting cracks, abutting against the older joints. These most recently formed joint sets show various patterns along the beach on different beds, due to their relative position to folds or the thickness of the underlying shale horizons (Engelder and Peacock, 2001). All joints generally terminate at the limestone-shale boundaries due to differences in mechanical properties of the two lithologies (Belayneh and Cosgrove, 2004).

The outcrop studied here (51°12′7.44″N, 3°11′55.27″W) is located 1.21 km west of the beach parking area and 0.27 km east of the military tower (Figure 1). It consists of a $20\times25$ m rectangle located at the eastern edge of the hinge of the Lilstock buttress anticline described by Engelder and Peacock (2001), on the upper part of the wave-cut platform, seaward of the boulders at the foot of the cliff. The outcrop is comprised of two 15 cm thick horizontal beds of limestone containing vertical fractures, overlying a layer of shale. It contains one main set of subvertical joints, broadly striking east–west (Figure 2). These joints are consistent with the Alpine joints described by Belayneh and Cosgrove (2004), which are located in the hinge region of the Lilstock anticline and are subparallel to the fold axis (see Figure 3 from Engelder and Peacock, 2001). A secondary set of smaller joints, with no defined preferred orientation, is also visible. They generally do not cross cut the main fractures and are partially or totally cemented. For the purpose of this chapter, we use the term "fracture" to refer to the east–west sets of long joints, and the term "crack" to describe the intermediate set of short joints.

## Data acquisition

### *Fracture mapping*

The outcrop of interest was mapped using a drone to obtain a detailed map of the joints. In total, 56 aerial photographs were acquired using a DJI Phantom 3 Standard drone, equipped with a 12 megapixel built-in camera installed on a stabilization gimbal. The photographs were merged to create a georeferenced orthomosaic of the wave-cut platform (Figure 3a). We manually digitized the cracks and fractures outcropping at the surface of the seismic survey area (Figure 3b). The rose diagram highlights the dominance of the long fractures striking in the east–west direction. Although short cracks are present at every angle, they exhibit a slight alignment in the north–south direction. The distribution of cracks is heterogeneous, with the top half of the survey area showing an intensity one order of magnitude larger than that in the bottom half of the sampled rectangle. Large areas without cracks and fractures also appear on the map. This is an artifact caused by the presence of boulders and water that make the mapping of the fractures and cracks impossible based on the aerial photograph. We observed different joint apertures on site, which varies between 3 and 4 mm for the cracks, to approximately 5 mm for the long fractures striking east–west. These apertures remain at the layers' depth. Fractures extending outside the delineated rectangle were cropped.

### *Seismic data set*

The seismic survey was conducted on 21 September 2016. According to the tide table for the Watchet Harbour Marina, located 10 km west of Lilstock, on this day, high and low tides occurred at 10:21 and 16:19, respectively. We acquired the surveys at 13:45, 15:10, and 17:25. Our outcrop of interest was submerged at high tide.

We acquired each seismic survey using compressional (P) and horizontal S-wave ($S_H$) sources. The surveys followed the method described by Hobday and Worthington (2012) and adapted by Foord et al. (2015), but with the additional acquisition of S-waves. A grid of 16 pairs of geophones ($4 \times 4$) was set up on a $15 \times 15$ m with 5 m spacing (Figure 4). Each pair is composed of a vertical and a horizontal geophone, recording P- and S-waves, respectively. To couple the geophones to the bare rock, we equipped the geophones with flat bases and glued them onto the rock using CrystalBond. It is melted to get a viscous couplant, which can then be applied to the geophones base. We used a simple camp stove because the material melts at approximately 60°C. It then solidifies and stiffens very rapidly, which allows the geophones to be firmly fixed to the rock. It is easily removable and dissolves in water. The horizontal geophones were oriented in the north–south direction, normal to the main fractures.

Seismic shots were distributed across 16 locations around the geophone grid, to cover the whole range of azimuths. Although hammer shots were performed directly on the bare rock to generate P-waves, we generated S-waves using a "Kirk" source (Hasbrouck, 1977). At every shot location, the source was oriented in the north–south direction, parallel to the horizontal geophones. The seismic traces were recorded using a Geometrics 24-channel Geode seismic recorder, within a sampling rate of 0.10 ms. Vertical and horizontal geophones had a 10 and 4.5 Hz dominant frequency, respectively. We transformed the raw waveforms into seismic velocities using manual picking of first arrivals, and distances calculated from the source-geophone grid geometry.

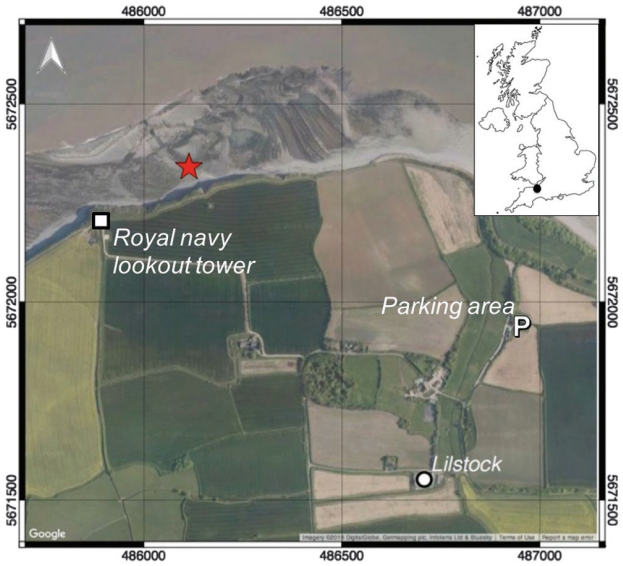


**Figure 1.** Location of our study site (the red star) on the coast of Somerset, South West England.

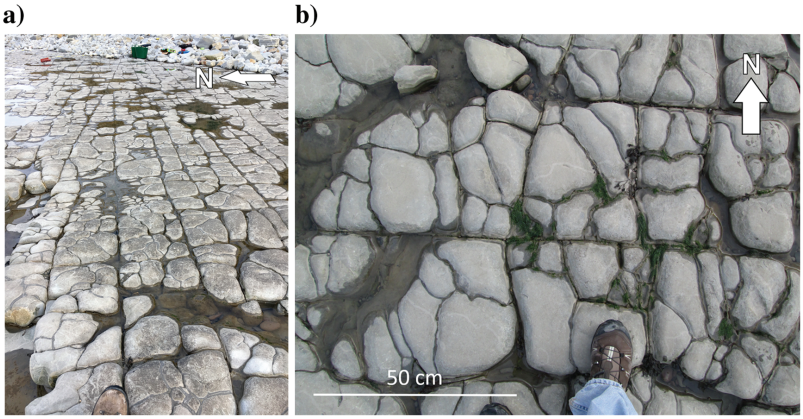


**Figure 2.** Fracture sets outcropping at the Lilstock wave-cut platform. (a) Long fractures striking east–west. (b) Short cracks with no well-defined preferred orientation. Shoes for scale.

Time-lapse surveys were repeated using the same geophone and source locations to ensure consistency in the acquisition between the three surveys. Any differences between the resulting velocities can thus be attributed to the changing saturation of the rock as the tide receded from the outcrop. The recorded P-wave seismogram (Figure 5a) shows little noise, and manual picking of the first arrivals was achieved for more than 95% of the 256 recorded traces. Cases in which sources are at the same location as geophones (1, 2, 3, and 4) are not used in the analysis. Due to the geometry of the grid, not all horizontal geophones recorded pure $S_H$-waves. To avoid P to $S_V$ conversion, we pick S-waves only when the ray azimuth is between 45° and 135° from north. Furthermore, the S-waves recorded by the horizontal geophones are much noisier than the P-wave records (Figure 5b). As a consequence, only 33% of the $S_H$-wave first arrivals are picked by visual inspection.

## Results

The P-wave velocities show a maximum at approximately 90° from north (Figure 6). The pattern of the $S_H$-wave velocities is less clear, mainly due to less data and the narrower maximum-minimum range expected for horizontal S-waves (Hall, 2000). Nevertheless, a minimum at approximately 90° from north and maximum near 45° and 135° from north is visible.

To identify the best-fitting model, we perform an inversion for the values of $Z_N$ and $Z_T$ that minimize the rms misfit between the observed and synthetic velocities (Table 1). This best-fitting model consists of a single fracture set, fixed at an orientation of 90°, consistent with the drone survey. The uncertainties in Table 1 are estimated by applying an $F$-test to the misfit surface (misfit as a function of each parameter). The background rock is assumed to be isotropic, with a velocity equal to the highest measured mean velocity, 2750 m/s. The background density was calculated using the Gardner's relation (Gardner et al., 1974), giving a value of 2250 kg/m$^3$. Gardner's relation is generally considered as a good approximation, although some scattering in real data may be observed around the estimated density (Nwozor et al., 2017). Thus, it is common to observe a

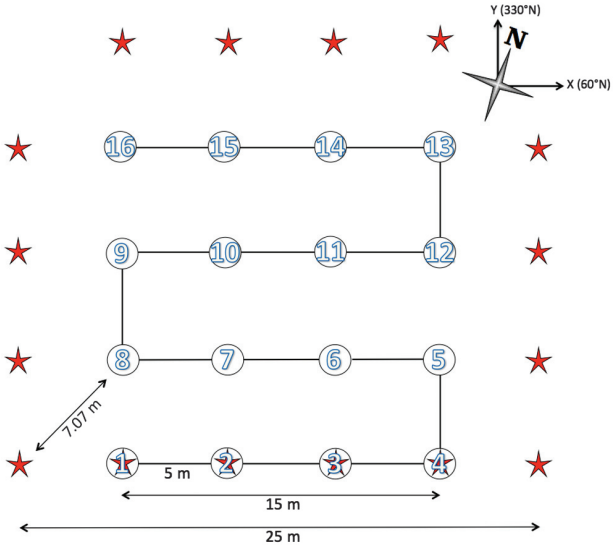


**Figure 4.** Configuration of the seismic surveys. Pairs of geophones are represented by the numbered circles, and hammer source locations are represented by the red stars.

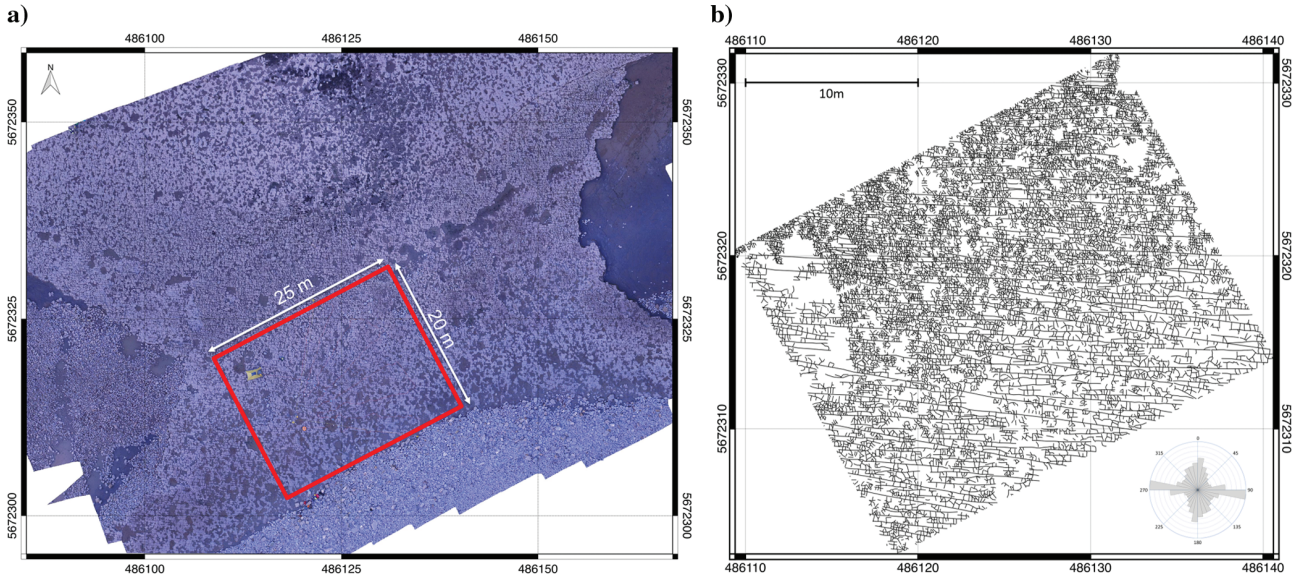


**Figure 3.** (a) Orthomosaic of the Lilstock outcrop acquired by the drone. (b) Fracture traces corresponding to the area of the seismic survey (the red rectangle in the left panel). The inserted rose diagram shows the orientation of the fracture and crack branches in degrees from north, normalized and weighted on the length. Note that the thickness of the lines is not true to scale and overestimates the width of the fractures and cracks.

considerable scattering of real data around the Gardner curve in many plots. This generalization is often a source of errors in some empirical studies (e.g., pore pressure analysis, reservoir characterization, top seal identification, and geomechanical studies) that require us to work with lithology-specific functions.

Despite the single-velocity maximum in our observations, we also tested rock-physics models with two orthogonal sets of fractures, showing two velocity maximums (Figure 6a). To approximate the velocity observation with two sets of orthogonal fractures, we needed to add a north–south set with $Z_N/Z_T \approx 0$, which corresponds to filled and poorly connected cracks.

## Discussion

### *Seismic velocities versus azimuth*

The observed patterns in velocity are better recovered using a rock-physics model containing a single set of aligned fractures striking east–west. The P-wave velocities show a maximum in the plane parallel to the fracture face and a minimum in the normal direction, which is consistent with previous observations (Crampin et al., 1980; Nunn et al., 1983; Hobday and Worthington, 2012). This model is also consistent with the pattern of the $S_H$-wave velocities (Hall, 2000). The main fracture set observed in the field is assumed to be the dominant factor influencing the anisotropy. Due to these fracture dimensions (average length approximately 4.7 m and spacing less than 0.5 m), the effective medium theory can be used to describe the seismic anisotropy (Ding et al., 2020). The secondary cracks are randomly oriented and reduce the seismic velocities in all directions. In comparison, Foord et al. (2015) record P-wave velocities up to 3500 m $s^{-1}$ in a limestone bed located 150 m northward from the study area.

A few P-wave propagation angles do not satisfy the best-fit models (6.9°, 96.9°, and 113.1° north), but these directions contain few data in comparison with the

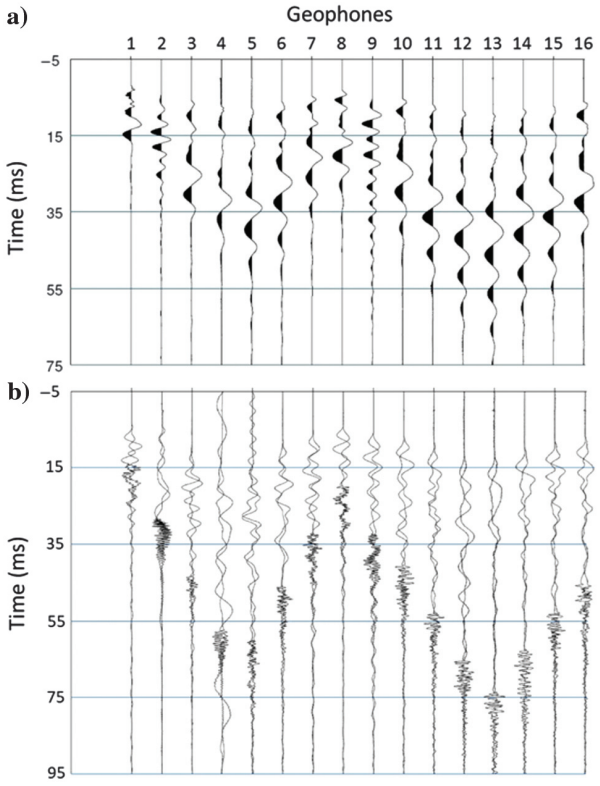


**Figure 5.** Raw traces recorded by (a) vertical and (b) horizontal geophones corresponding to the first shot (the red star at the bottom left location on Figure 4) from the first P- and S-wave surveys. First arrivals are marked by the red scores. The geophone numbers refer to Figure 4.

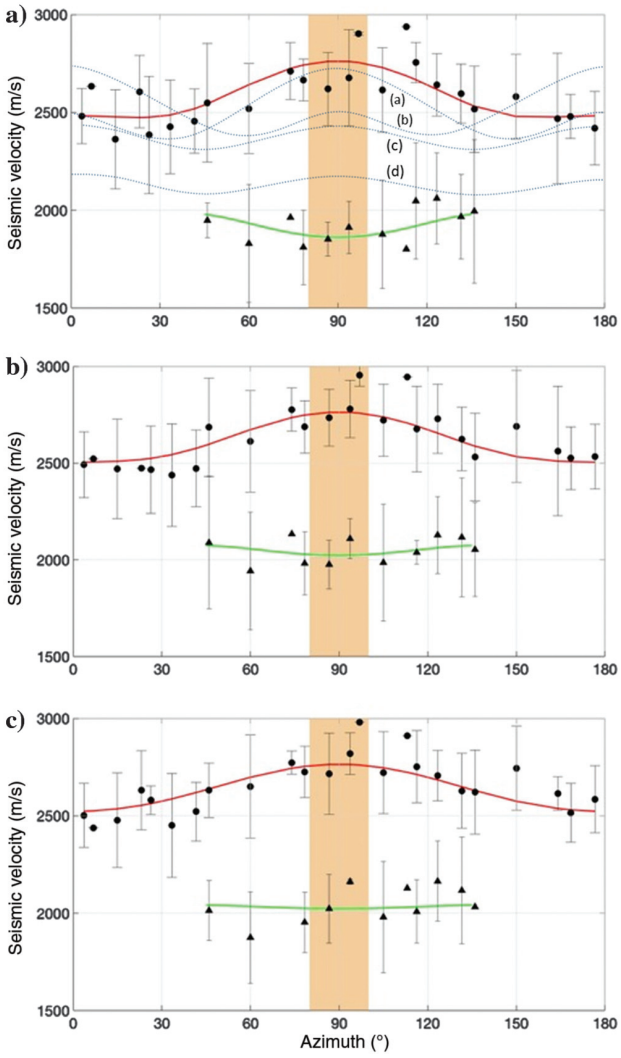


**Figure 6.** Measured P- (the black dots) and $S_H$-wave velocities (the black triangles) on the Lilstock outcrop. Surveys realized at (a) 13:45, (b) 15:10, and (c) 17:25. Error bars represent one standard deviation of the measured velocities. The red and green curves show the best-fitting modeled velocities for the P- and $S_H$-waves, respectively (Table 1). The orange-shaded area represents the range of strikes of the main fracture set. The dotted lines labeled (a-d) on the top panel show modeled velocities using parameters indicated in the inset box.

other azimuths and are considered to be less representative of the overall anisotropy. The model assumes homogeneity in fracture compliance and matrix velocities, whereas some lateral variation is likely to be expected across the survey area, as revealed with the drone survey. Such heterogeneity is also responsible for the significant scattering present in the data. Hobday and Worthington (2012) attribute these errors to three major causes, the first one being error in picking the first arrivals. Due to the particularly clear signal, we assume this to be relatively low. The second cause is the likely variation of fracture compliance over the surveyed area. Some variation in crack density and aperture was observed on the grid. The third cause of scatter is lateral variations in the rock matrix velocity. After carrying out the survey at Lilstock, a fourth possible cause of scatter being of a geometric nature was identified. The in situ position of the geophones and source points slightly deviate from the idealized grid (Figure 4) used to perform the traveltime to velocity transform. Nevertheless, it is expected that the heterogeneity of the fracture system, and particularly the heterogeneity in the fracture intensity observed on the outcrop (Figure 3), is the dominant source of error.

**Table 1. Fracture compliance parameters.**

| | Survey 1 | Survey 2 | Survey 3 |
|---|---|---|---|
| | 13:45 | 15:10 | 17:25 |
| $Z_N/Z_T$ | $0.20 \pm 0.08$ | $0.42 \pm 0.10$ | $0.46 \pm 0.11$ |
| $Z_N$ ($\times 10^{-11}$ 1/Pa) | $1.28 \pm 0.43$ | $1.44 \pm 0.25$ | $1.26 \pm 0.23$ |
| $Z_T$ ($\times 10^{-11}$ 1/Pa) | $6.38 \pm 1.09$ | $3.43 \pm 0.56$ | $2.73 \pm 0.43$ |

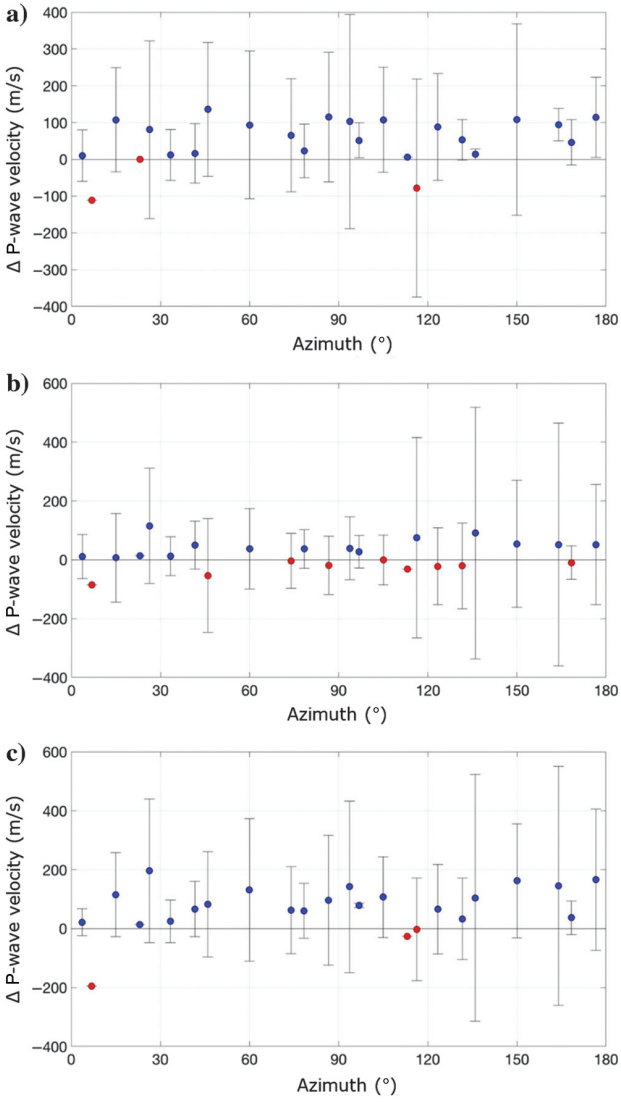


**Figure 7.** The P-wave velocity variation for each measured angle of propagation between (a) survey 1 (13:45) and survey 2 (15:10), (b) survey 2 (15:10) and survey 3 (17:25), and (c) survey 1 (13:45) and survey 3 (17:25). The blue and red dots show positive and negative trends, respectively.

### *Velocity changes*

The change in P-wave velocities from survey 1 to survey 3 is positive for almost every direction of propagation (Figure 7). We observe an increase of up to 8%. Two of the three azimuths (6.9° and 23.1°) that show a reduction in velocity are angles with fewer data points, whereas the third (116.3°) shows almost zero change. Most of the changes occur between the first two surveys (Figure 7a); the change between surveys 2 and 3 is less significant.

The velocity increase indicates a change in the properties of the fractured outcrop, most likely associated with the tide going out during the seismic experiment and the drainage of the rock mass and fractures. An increase in the seismic velocities as the tide recedes is counterintuitive because typically the substitution of a stiffer fluid (water) by a softer fluid (air) is associated with a velocity increase. However, this effect is typically observed when a rock is initially 100% saturated by the stiff fluid. The first survey was conducted approximately 3 h after high tide (whereas a shorter time would have been preferable, safety and logistical constraints prevented us from accessing the site any earlier), and so a portion of the rock must have already drained. Figure 8 shows the impact of water versus air saturation on P-wave velocities that we calculated using Gassmann's equation (Gassmann, 1951). With a very large contrast in the fluid properties between water and air, the impact of a change in fluid saturation will be significant. The overall bulk modulus of a fluid mixture is given by the harmonic mean (i.e., the Reuss average). As such, with only a very small amount of air in the fluid mixture, the bulk modulus becomes essentially that of air. However, the overall density of the fluid mixture is

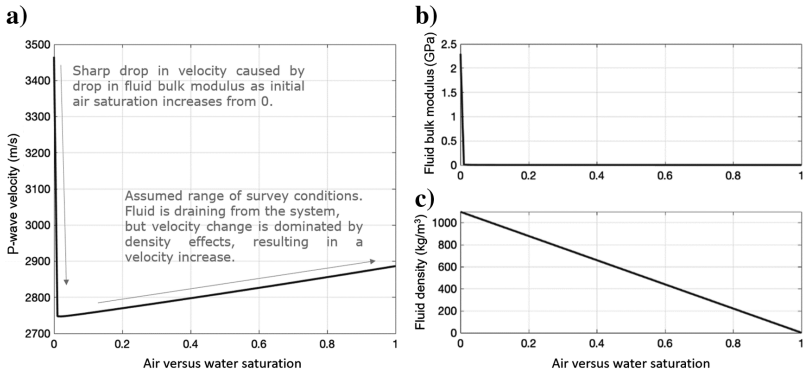


**Figure 8.** (a) Modeled P-wave velocity change as a function of water versus air saturation (using the bulk modulus and density of 2.3 GPa and 1100 kg/m$^3$ for seawater and 100 kPa and 1.3 kg/m$^3$ for air), using Gassmann's equation, assuming a porosity of 20% and a mineral bulk modulus of 70 GPa (calcite). (b and c) We show the change in bulk modulus and density of the combined fluid. The fluid bulk modulus decreases rapidly for a small amount of air saturation because it is computed using a harmonic mean (Reuss average), whereas the density, computed using an arithmetic mean, shows a gradual change. The impact on the rock seismic velocity is that a large decrease caused by the drop in bulk modulus occurs over the first few percent of air saturation, after which a velocity increase, caused by the density decrease, occurs. Here, we model an increase in velocity with air saturation of approximately 140m/s, from 2750 to 2990m/s, a similar order to that observed for our data.

determined by the arithmetic mean of the two fluids, which means that the density evolves gradually with fluid saturation. Therefore, as the saturation of air increases from zero, the velocity reduction produced by the drop in the fluid mixture bulk modulus occurs over the first few percentage points of saturation. From this point onward, increasing the air saturation of more than a few percent at the point of the first survey, which is reasonable given that this was performed 3 h after high tide, further loss of water will act to increase the velocities, as observed here.

### *Fracture compliance*

We find a doubling of Ω from 0.20 to 0.42 between the first and second survey, as the rock evolves from partially saturated to mostly drained conditions (Table 1). Laboratory experiments made on core and synthetic samples have shown that Ω tends to increase as a stiff fluid is replaced by a softer one (Pyrak-Nolte et al., 1990; Hsu and Schoenberg, 1993; Sayers, 1999; Lubbe et al., 2008). However, an increase in Ω caused by saturation changes is typically interpreted as being caused by an increase in $Z_N$ because, assuming penny-shaped fractures, the latter is sensitive to the fluid bulk modulus, whereas $Z_T$ is sensitive only to the fluid shear modulus, which is zero for water and gas (e.g., Pointer et al., 2000). However, for our study, the increase in Ω was caused by a decrease in $Z_T$, and not by an increase in $Z_N$ (Table 1). Our conjecture is that the fractures are not entirely fluid filled but contain other filling materials such as clay minerals (Janos Urai, personal communication), which acts as a lubricant when combined with water (Odom, 1984; Schleicher et al., 2006; Tembe et al., 2010), and potentially detritus and algal material as well. The loss of water causes the clay to harden, reducing its ability to slide, and therefore increasing the shear stiffness of the fractures.

Although this hypothesis is untested, our observations show the need for caution when interpreting observations of anisotropy under the assumption of debris-free, smooth penny-shaped cracks: In reality, they are likely to exhibit significant roughness and asperities and often exhibit mineralization, creating bridges between fracture faces (Sayers et al., 2009), and so the penny-shaped models may not apply.

## Conclusion

Three pairs of P- and S-wave refraction seismic surveys were carried out on a fractured wave-cut platform located on the coast of Somerset, UK. The surveys were performed over a period of time when the tide was going out and the fractures were draining. The site exhibits a strong seismic anisotropy caused by the presence of a single dominant set of aligned east–west-trending fractures. An increase of the seismic velocities as the tide recedes is attributed to the lower density air replacing relatively denser liquids in the fractures. Furthermore, an increase in the fracture compliance ratio (Ω) is observed, mainly due to a drop of the tangential component ($Z_T$).

Azimuthal seismic surveys using P-waves are useful to determine fracture orientation, as well as changes in fracture saturation. They provide insights into fracture mechanisms at the field scale. Fractured outcrops near the shoreline and influenced by tide cycles provide good sites to develop techniques for fracture imaging. Unlike the laboratory experiments, field surveys are not fully constrained, and some assumption must be made to interpret the results. A good example is the assumptions of rock and fracture homogeneity across the field site. In our case, a drone survey helped to interpret the seismic results. Further experiments are required to investigate the impact of these heterogeneities on our results. It would also be worth expanding the study area to investigate issues of upscaling from outcrop to the reservoir scale and the impact on the seismic properties thereof.

## Acknowledgments

The authors want to thank A. Butcher, A. Stork, T. Tessema, J. Walpole, and A. Williams from the University of Bristol for their support on the field. The $S_H$-wave source was designed in collaboration with the workshop of the School of Earth Sciences of the University of Bristol. This project has received funding from the European Union's Horizon 2020 research

and innovation programme under the Marie Skłodowska Curie grant agreement no. 642029 and from the SHAPE-UK Unconventional Hydrocarbons NERC grant no. NE/R018006/1. The Centro de Estudios Científicos (CECs) is cofunded by the Base Finance program of ANID/PIA APOYO CCTE AFB170003.

## Data and materials availability

Data associated with this research are available and can be obtained by contacting the corresponding author.

## References

Al-Harrasi, O. H., J. M. Kendall, and M. Chapman, 2011, Fracture characterization using frequency-dependent shear wave anisotropy analysis of microseismic data: Geophysical Journal International, **185**, 1059–1070, doi: 10.1111/j.1365-246X.2011.04997.x.

Angus, D. A., J. P. Verdon, Q. J. Fisher, and J. M. Kendall, 2009, An audit of dry-core velocity-stress measurements: Geophysics, **74**, no. 5, E193–E203, doi: 10.1190/1.3183940.

Bakulin, A., 2003, Intrinsic and layer-induced vertical transverse isotropy: Geophysics, **68**, 1708–1713, doi: 10.1190/1.1620644.

Bakulin, A., V. Grechka, and I. Tsvankin, 2000, Estimation of fracture parameters from reflection seismic data — Part 1: HTI model due to a single fracture set: Geophysics, **65**, 1788–1802, doi: 10.1190/1.1444863.

Belayneh, M., and J. W. Cosgrove, 2004, Fracture-pattern variations around a major fold and their implications regarding fracture prediction using limited data: An example from the Bristol Channel Basin, *in* J. W. Cosgrove and T. Engelder, eds., The initiation, propagation, and arrest of joints and other fractures: Geological Society, London, Special Publications, 89–102.

Choi, M.-K., A. Bobet, and L. J. Pyrak-Nolte, 2014, The effect of surface roughness and mixed-mode loading on the stiffness ratio for fractures: Geophysics, **79**, no. 5, D319–D331, doi: 10.1190/geo2013-0438.1.

Crampin, S., R. McGonigle, and D. Bamford, 1980, Estimating crack parameters from observations of P-wave velocity anisotropy: Geophysics, **45**, 345–360, doi: 10.1190/1.1441086.

Dart, C. J., K. McClay, and P. N. Hollings, 1995, 3D analysis of inverted extensional fault systems, southern Bristol Channel Basin, UK: Geological Society, London, Special Publications 88, 393–413.

Ding, P., D. Wang, and X. Y. Li, 2020, An experimental study on scale dependent velocity and anisotropy in fractured media based on artificial rocks with controlled fracture geometries: Rock Mechanics and Rock Engineering, **53**, 3149–3159, doi: 10.1007/s00603-020-02095-2.

Engelder, T., and D. C. P. Peacock, 2001, Joint development normal to regional compression during flexural-flow folding: The Lilstock buttress anticline, Somerset, England: Journal of Structural Geology, **23**, 259–277, doi: 10.1016/S0191-8141(00)00095-X.

Far, M. E., J. J. S. de Figueiredo, R. R. Stewart, J. P. Castagna, D.-H. Han, and N. Dyaur, 2014, Measurements of seismic anisotropy and fracture compliances in synthetic fractured media: Geophysical Journal International, **197**, 1845–1857, doi: 10.1093/gji/ggu101.

Foord, G., J. P. Verdon, and J. M. Kendall, 2015, Seismic characterization of fracture compliance in the field using P- and S-wave sources: Geophysical Journal International, **203**, 1726–1737, doi: 10.1093/gji/ggv395.

Gardner, G. H. F., L. W. Gardner, and A. R. Gregory, 1974, Formation velocity and density — The diagnostic basics for stratigraphic traps: Geophysics, **39**, 770–780, doi: 10.1190/1.1440465.

Gassmann, F., 1951, Uber die elastizitat poroser medien: Vierteljahresschrift der Naturforschenden Gesellschaft in Zurich, **96**, 1–23.

Hall, S. A., 2000, Rock fractures characterisation and seismic anisotropy: Application to ocean bottom seismic data: Ph.D. thesis, University of Bristol.

Harris, S. D., Q. J. Fisher, M. Karimi-Fard, A. Z. Vaszi, and K. Wu, 2005, Modelling the effects of faults and fractures on fluid flow in petroleum reservoirs, Transport phenomena in porous media III: Pergamon, 441–476.

Hasbrouck, W. P., 1977, Working drawings of a Kirk shear wave source: U.S. Geological Survey Open-File Report 77-622: Technical report, United States Geological Survey.

Hobday, C., and M. H. Worthington, 2012, Field measurements of normal and shear fracture compliance: Geophysical Prospecting, **60**, 488–499, doi: 10.1111/j.1365-2478.2011.01000.x.

Hsu, C.-J., and M. Schoenberg, 1993, Elastic waves through a simulated fractured medium: Geophysics, **58**, 964–977, doi: 10.1190/1.1443487.

Johansen, T. A., B. O. Ruud, and M. Jakobsen, 2004, Effect of grain scale alignment on seismic anisotropy and reflectivity of shales: Geophysical Prospecting, **52**, 133–149, doi: 10.1046/j.1365-2478.2003.00405.x.

Jupe, A. J., R. H. Jones, S. A. Wilson, and J. F. Cowles, 2003, Microseismic monitoring of geomechanical reservoir processes and fracture-dominated fluid flow: Geological Society, London, Special Publications 209, 77–86.

Kendall, J. M., Q. J. Fisher, S. C. Crump, J. Maddock, A. Carter, S. A. Hall, J. Wookey, S. L. A. Valcke, M. Casey, G. Lloyd, and W. B. Ismail, 2007, Seismic anisotropy as an indicator of reservoir quality in siliciclastic rocks: Geological Society, London, Special Publications 292, 123–136.

Kendall, J. M., J. P. Verdon, A. Baird, A. Wuestefeld, and J. T. Rutledge, 2012, Microseismic monitoring of fracture networks during hydraulic stimulation: Beyond event locations: Society of Petroleum Engineers.

Khelifa, C., A. Zeddouri, and F. Djabes, 2014, Influence of natural fractures on oil production of unconventional

reservoirs: Energy Procedia, **50**, 360–367, doi: 10.1016/j.egypro.2014.06.043.

Lubbe, R., J. Sothcott, M. H. Worthington, and C. Mccann, 2008, Laboratory estimates of normal and shear fracture compliance: Geophysical Prospecting, **56**, 239–247, doi: 10.1111/j.1365-2478.2007.00688.x.

Lynn, H., and L. Thomsen, 1990, Reflection shear-wave data along the principal axes of aximuthal anisotropy: Geophysics, **55**, 147–156, doi: 10.1190/1.1442821.

Macbeth, C., and H. Schuett, 2007, The stress dependent elastic properties of thermally induced microfractures in aeolian Rotliegend sandstone: Geophysical Prospecting, **55**, 323–332, doi: 10.1111/j.1365-2478.2007.00601.x.

Nemčok, M., R. Gayer, and M. Miliorizos, 1995, Structural analysis of the inverted Bristol Channel Basin: Implications for the geometry and timing of fracture porosity: Geological Society, London, Special Publications 88, 355–392.

Nunn, K. R., R. D. Barker, and D. Bamford, 1983, In situ seismic and electrical measurements of fracture anisotropy in the Lincolnshire Chalk: Quarterly Journal of Engineering Geology and Hydrogeology, **16**, 187–195, doi: 10.1144/GSL.QJEG.1983.016.03.03.

Nwozor, K. K., L. O. Onuorah, S. O. Onyekuru, and C. J. Egbuachor, 2017, Calibration of Gardner coefficient for density–velocity relationships of tertiary sediments in Niger Delta Basin: Journal of Petroleum Exploration and Production Technology, **7**, 627–635, doi: 10.1007/s13202-017-0313-7.

Odom, I. E., 1984, Smectite clay minerals: Properties and uses: Philosophical Transactions of the Royal Society of London A, **311**, 391–409, doi: 10.1098/rsta.1984.0036.

Pointer, T., E. Liu, and J. A. Hudson, 2000, Seismic wave propagation in cracked porous media: Geophysical Journal International, **142**, 199–231, doi: 10.1046/j.1365-246x.2000.00157.x.

Pyrak-Nolte, L. J., L. R. Myer, and N. G. Cook, 1990, Transmission of seismic waves across single natural fractures: Journal of Geophysical Research, **95**, 8617–8638, doi: 10.1029/JB095iB06p08617.

Rathore, J. S., and E. Fjaer, 1994, P- and S-wave anisotropy of a synthetic sandstone with controlled crack geometry: Geophysical Prospecting, **43**, 711–728, doi: 10.1111/j.1365-2478.1995.tb00276.x.

Sayers, C. M., 1999, Stress-dependent seismic anisotropy of shales: Geophysics, **64**, 93–98, doi: 10.1190/1.1444535.

Sayers, C. M., A. D. Taleghani, and J. Adachi, 2009, The effect of mineralization on the ratio of normal to tangential compliance of fractures: Geophysical Prospecting, **57**, 439–446, doi: 10.1111/j.1365-2478.2008.00746.x.

Schleicher, A. M., B. A. Van Der Pluijm, J. G. Solum, and L. N. Warr, 2006, Origin and significance of clay-coated fractures in mudrock fragments of the SAFOD borehole (Parkfield, California): Geophysical Research Letters, **33**, 1–5, doi: 10.1029/2006GL026505.

Schoenberg, M., and C. M. Sayers, 1995, Seismic anisotropy of fractured rock: Geophysics, **60**, 204–211, doi: 10.1190/1.1443748.

Stork, A. L., J. P. Verdon, and J. M. Kendall, 2015, The microseismic response at the In Salah Carbon Capture and Storage (CCS) site: International Journal of Greenhouse Gas Control, **32**, 159–171, doi: 10.1016/j.ijggc.2014.11.014.

Tang, C., J. A. Rial, and J. M. Lees, 2005, Shear-wave splitting: A diagnostic tool to monitor fluid pressure in geothermal fields: Geophysical Research Letters, **32**, 1–3, doi: 10.1029/2005GL023551.

Teanby, N., J.-M. Kendall, R. H. Jones, and O. Barkved, 2004, Stress-induced temporal variations in seismic anisotropy observed in microseismic data: Geophysical Journal International, **156**, 459–466, doi: 10.1111/j.1365-246X.2004.02212.x.

Tembe, S., D. A. Lockner, and T. F. Wong, 2010, Effect of clay content and mineralogy on frictional sliding behavior of simulated gouges: Binary and ternary mixtures of quartz, illite, and montmorillonite: Journal of Geophysical Research, Solid Earth, **115**, 1–22, doi: 10.1029/2009JB006383.

Valcke, S. L. A., M. Casey, G. E. Lloyd, J. M. Kendall, and Q. J. Fisher, 2006, Lattice preferred orientation and seismic anisotropy in sedimentary rocks: Geophysical Journal International, **166**, 652–666, doi: 10.1111/j.1365-246X.2006.02987.x.

Van Hoorn, B., 1987, The south Celtic Sea/Bristol Channel Basin: Origin, deformation and inversion history: Tectonophysics, **137**, 309–334, doi: 10.1016/0040-1951(87)90325-8.

Verdon, J. P., and J. M. Kendall, 2011, Detection of multiple fracture sets using observations of shear-wave splitting in microseismic data: Geophysical Prospecting, **59**, 593–608, doi: 10.1111/j.1365-2478.2010.00943.x.

Verdon, J. P., J. M. Kendall, and A. Wüstefeld, 2009, Imaging fractures and sedimentary fabrics using shear wave splitting measurements made on passive seismic data: Geophysical Journal International, **179**, 1245–1254, doi: 10.1111/j.1365-246X.2009.04347.x.

Verdon, J. P., and A. Wüstefeld, 2013, Measurement of the normal/tangential fracture compliance ratio (ZN/ZT) during hydraulic fracture stimulation using S-wave splitting data: Geophysical Prospecting, **61**, 461–475, doi: 10.1111/j.1365-2478.2012.01132.x.

Vlahovic, G., M. Elkibbi, and J. A. Rial, 2003, Shear-wave splitting and reservoir crack characterization: The Coso geothermal field: Journal of Volcanology and Geothermal Research, **120**, 123–140, doi: 10.1016/S0377-0273(02)00368-2.

Walker, A. M., and J. Wookey, 2012, MSAT — A new toolkit for the analysis of elastic and seismic anisotropy: Computers and Geosciences, **49**, 81–90, doi: 10.1016/j.cageo.2012.05.031.

Worthington, M. H., and R. Lubbe, 2007, The scaling of fracture compliance, *in* L. Lonergan, L. Jolly, R. Rawnsley, and D. Sanderson, eds., Fractured reservoirs: Geological Society of London, 73–82.

Wuestefeld, A., J. M. Kendall, J. P. Verdon, and A. Van As, 2011, In situ monitoring of rock fracturing using shear wave splitting analysis: An example from a mining setting: Geophysical Journal International, **187**, 848–860, doi: 10.1111/j.1365-246X.2011.05171.x.

Xia, J., R. A. Falconer, and B. Lin, 2010, Impact of different tidal renewable energy projects on the hydrodynamic processes in the Severn Estuary, UK: Ocean Modelling, **32**, 86–104, doi: 10.1016/j.ocemod.2009.11.002.

Biographies and photographs of the authors are not available.